Journal of Materials Chemistry C

ROYAL SOCIETY OF CHEMISTRY

PAPER

View Article Online
View Journal | View Issue

Check for updates

Cite this: J. Mater. Chem. C, 2024, 12, 685

Host–guest complexes of perylene bisimide-based metallacage and fullerenes for efficient photoinduced charge separation†

O. A. Stasyuk, [a] M. Solà *[a] and A. J. Stasyuk *[ab]

Received 19th September 2023,
Accepted 2nd December 2023

DOI: 10.1039/d3tc03412g

rsc.li/materials-c

The discovery of coordination-driven self-assembly has greatly expanded the field of organic macrocyclic compounds. This approach enables the construction of precise supramolecular complexes, known as metallacages, assembled from organic ligands coordinated with metal centers. Metallacages come in various sizes and shapes, making them capable of hosting guest molecules of different sizes. In this work, we report the ground and excited state properties of non-covalent complexes between various fullerenes (C_{60}, C_{70}, $Sc_3N@C_{80}$, $Sc_3CH@C_{80}$, and $Sc_4O_3@C_{80}$) and Pt_6PBI_3 metallacage, composed of perylene bisimide units and organoplatinum nodes. These complexes exhibit thermodynamically favorable photoinduced charge transfer from endohedral metallofullerenes to metallacage that occurs within picoseconds. Among the systems considered, the $Pt_6PBI_3 \supset Sc_3N@C_{80}$ complex stands out as the most promising candidate for use in photovoltaics due to its ability for fast charge separation and slow charge recombination.

Introduction

Organic macrocyclic compounds, such as crown ethers,[1] cryptands,[2] and cavitands[3,4] became widespread and firmly established in the routine life of chemists almost immediately after their discovery.[5] Due to their ability to engage in multiple non-covalent interactions and selectively bind small cationic species, they are widely used as phase transfer catalysts,[6,7] specific metal cation sensors,[8,9] or even as compounds that facilitate ion transport across cell membranes (ionophore) in biological applications.[10] Cyclodextrins are another type of macrocyclic compound composed of glucopyranoside sugar molecules bound together in rings of various sizes. Depending on their size, they can accommodate neutral or charged molecules.[11] This ability, in combination with very low toxicity, allows cyclodextrins to find broad applications as drug delivery agents in numerous official approved medicines.[12–14] However, due to the narrow cavity size, their host–guest chemistry is limited to small molecules and often has restricted use in polar protogenic environments. Porous organic cages[15] with shape-stable structures are of particular interest in supramolecular chemistry due to their internal cavities of different size and ability to bind to guest molecules, such as fullerenes.[16–18] Charge-separated states with long lifetimes were observed in porphyrin-based organic cages with encapsulated C_{60}/C_{70} fullerenes.[17,19]

The discovery of coordination-driven self-assembly has significantly expanded host–guest chemistry.[20–22] This powerful tool allows for precise construction of supramolecular complexes, such as metal–organic cages or metallacages, in various shapes and sizes.[23,24] Metal–organic cages are molecular assemblies of organic ligands coordinated with either metal cations or metal oxide clusters of different nuclearities, resulting in architectures with inherent porosity. Similar to other macrocyclic compounds, metal–organic cages are capable of binding various organic guests. At the same time, since the size and shape of metal–organic cages can vary broadly, the size of the guest molecule can also differ significantly.[25,26]

Since the majority of metallacages are constructed from rigid organic fragments, enhancing non-covalent interactions is a natural approach to facilitate their hosting ability.[27,28] Therefore, the ideal building blocks for preparation of metallacages with promising host–guest chemistry are extended π-conjugated organic ligands, such as polycyclic aromatic hydrocarbons,[29–31] porphyrins,[32–36] or rylene bisimides.[37–40]

[a] Institut de Química Computacional i Catàlisi and Departament de Química, Universitat de Girona, C/ Maria Aurèlia Capmany 69, 17003 Girona, Catalonia, Spain. E-mail: miquel.sola@udg.edu, antony.stasuk@gmail.com
[b] Faculty of Chemistry, University of Warsaw, Pasteura 1, 02-093 Warsaw, Poland

† Electronic supplementary information (ESI) available: Supporting information is available and includes a detailed computational methodology, characteristics of interactions between fullerenes and metallacage (QTAIM, NCI, and energy decomposition data), charge separation values and rates of photoinduced electron transfer. Cartesian coordinates for all studied systems are also provided. See DOI: https://doi.org/10.1039/d3tc03412g

In 2013, Würthner and co-workers first synthesized and characterized a giant tetrahedral host (M_4L_6), assembled from octahedral Fe(II) ions and linear perylene bisimide (**PBI**) dyes with 2,2′-bipyridine groups.[41] The reported cage, with an edge length of 3.9 nm and an estimated internal volume of more than 950 Å^3, exhibits broad and strong absorption in the visible region (up to 650 nm). Moreover, it demonstrates a total of 7 highly reversible electrochemical oxidation and reduction waves. The ability to encapsulate $\mathbf{C_{60}}$ fullerene was demonstrated through UV-Vis and NMR spectroscopy, as well as mass spectrometry. It is important to note that spectroscopic measurements suggest that each cage can accommodate two fullerenes. The evolution of this work led to the synthesis of a structurally similar metallacage in which Fe(II) ions were replaced by Zn(II) ions.[42] This replacement dramatically enhanced the cage's fluorescence quantum yield. The new cage also demonstrates the ability to accommodate aromatic guests, coronene and perylene, with host–guest ratio of 1 : 2 and 1 : 3, respectively.

In 2020, Fang, Stang, and their co-workers reported a novel supramolecular complex constructed through the coordination-driven self-assembly of *o*-tetrapyridyl perylene bisimide with *cis*-$(PEt_3)_2Pt(OTf)_2$.[43] The synthesized metallacage ($\mathbf{Pt_6PBI_3}$) has the shape of a trigonal prism and possesses an inner cavity with a diameter of 14.7 Å. A cavity of this size is suitable for accommodating both $\mathbf{C_{60}}$ and $\mathbf{C_{70}}$ fullerenes, providing free rotation of the fullerenes inside it. However, as has been demonstrated, the cage exhibits a greater affinity towards $\mathbf{C_{70}}$. This, combined with the possibility of fabricating monomolecular membranes, opens up broad application perspectives for $\mathbf{Pt_6PBI_3}$ and its host–guest complexes.

In this work, we report a theoretical study of the electronic and photophysical properties of the host–guest complexes of $\mathbf{Pt_6PBI_3}$ and various fullerenes. We conduct a comprehensive analysis of the photoinduced electron transfer (PET) occurring in the complexes by means of DFT/TDA-DFT method. The obtained results show that the $\mathbf{Pt_6PBI_3}$ metallacage exhibits a strong electron acceptor nature. The complexes formed with fullerene guests can exhibit either intense fluorescence or pronounced PET properties.

Computational methods

Geometry optimizations were performed utilizing the DFT BLYP[44,45] exchange–correlation functional along with the empirical D3(BJ) dispersion correction[46,47] and def2-SVP basis set.[48,49] The calculations were performed within the ORCA 5.0.3 program.[50,51] Energy decomposition analysis (EDA) at BLYP-D3(BJ)/TZP level was performed using the Amsterdam density functional (ADF) program.[52] For electronic structure calculations and vertical excitation energies, the TDA formalism[53] with the range-separated CAM-B3LYP functional[54] and def2-SVP basis set[48,49] was employed in Gaussian 16 (rev. A.03).[55] Population analysis was performed within Mulliken,[56] Löwdin,[57] Hirshfeld,[58] and CM5[59] schemes. Solvent effects were accounted using a COSMO-like polarizable continuum model (C-PCM) with acetonitrile as a solvent (dielectric constant ε = 35.69).[60,61] Topological analysis of the electron density distribution was conducted using the "quantum theory of atoms in molecules" (QTAIM). Properties of electron density at the bond critical points (BCPs), such as electron density [$\rho(r)$], its Laplacian [$\nabla^2\rho(r)$], potential energy density [$V(r)$], kinetic energy density [$G(r)$], and total electron energy density [$H(r)$] were evaluated using the AIMALL suite.[62] Chemcraft 1.8 program[63] was utilized for molecular structures and frontier molecular orbitals visualization. Further methodological details, including analysis of excited states, calculation of electron transfer rates, reorganization and interaction energies are available in the ESI.†

Results and discussion

Ground state properties of Pt_6PBI_3 metallacage and its complexes with C_{60}/C_{70} fullerenes

The encapsulation of $\mathbf{C_{60}}$ and $\mathbf{C_{70}}$ fullerenes in $\mathbf{Pt_6PBI_3}$ metallacage was experimentally carried out in acetone solution and robustly confirmed by a combination of multinuclear NMR and mass-spectrometry.[43] A series of NMR measurements taken over an extended period of time for a very dilute solution of $\mathbf{Pt_6PBI_3 \supset C_{60}}$ and $\mathbf{Pt_6PBI_3 \supset C_{70}}$ complexes revealed no indication of complex instability. The electronic complementarity between the metallacage and fullerenes, along with their ability to undergo reversible electrochemical oxidation/reduction suggests strong electronic communication between the units in both ground and excited states. However, cyclic voltammetry and spectroscopic studies indicated that fullerene encapsulation has only a limited effect on the electronic nature of the metallacage, suggesting weak electronic communication between the host and guest units.

To gain deeper insights into the behavior of the $\mathbf{Pt_6PBI_3}$ metallacage and the fullerenes in their free state and within the corresponding host–guest complexes, a detailed comparison of their electronic properties was conducted. The optimized ground state (GS) geometries of the $\mathbf{Pt_6PBI_3 \supset C_{60}}$ and $\mathbf{Pt_6PBI_3 \supset C_{70}}$ complexes are shown in Fig. 1.

It is well known that fullerenes possess strong electron-acceptor properties. As depicted in Fig. 1, the lowest unoccupied molecular orbital (LUMO) of the metallacage is almost 1 eV lower in energy than LUMO of $\mathbf{C_{60}}$/$\mathbf{C_{70}}$, indicating its exceptionally strong electron-acceptor capabilities. In the $\mathbf{Pt_6PBI_3 \supset C_{60}}$ and $\mathbf{Pt_6PBI_3 \supset C_{70}}$ complexes, the LUMO remains localized on the cage, and its energy is nearly identical to that of the isolated metallacage. The nature of the highest occupied molecular orbital (HOMO) is somewhat different in the complexes with $\mathbf{C_{60}}$ and $\mathbf{C_{70}}$. In $\mathbf{Pt_6PBI_3 \supset C_{60}}$, the HOMO is delocalized over both host and guest units in a ratio of 0.64 : 0.36, respectively. Meanwhile, in $\mathbf{Pt_6PBI_3 \supset C_{70}}$, the degree of HOMO localization increases to a ratio of 0.88 : 0.12. Thus, the destabilization of the HOMO observed during the complex formation is attributed to its partial delocalization over the fullerene units. Given the strong electron-acceptor properties of the metallacage, we checked the charge

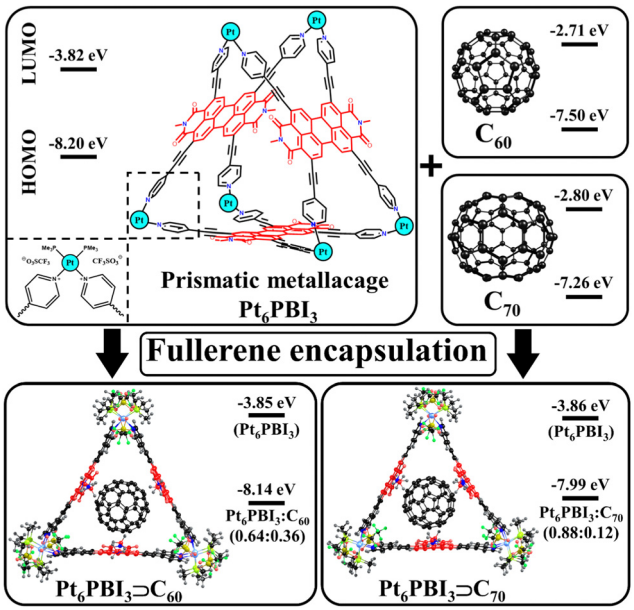

Fig. 1 Structure of $Pt_6PBI_3 \supset C_{60}$ and $Pt_6PBI_3 \supset C_{70}$ complexes. HOMO and LUMO energies of Pt_6PBI_3, C_{60}, and C_{70} in free state and in the corresponding complexes.

separation between host and guest units in the GS. However, population analysis performed within commonly used schemes did not reveal any significant charge transfer between the units, charge separation in GS does not exceed 0.1 *e* (Table S1, ESI†). Thus, the slight differences in orbital energies observed upon complexation, coupled with the absence of GS charge separation, validate the limited electronic communication between the metallacage and fullerenes, which has been previously observed in the electrochemical and spectroscopic studies.[43]

To assess the stability of the complexes, we calculated the interaction energy (ΔE_{int}) between the Pt_6PBI_3 cage and C_{60}/C_{70} units, as well as the deformation energy (ΔE_{def}) associated with the distortion of the units from their equilibrium geometries to the geometries they adopt in the complexes. For $Pt_6PBI_3 \supset C_{60}$ and $Pt_6PBI_3 \supset C_{70}$, ΔE_{int} is −61.5 and −78.3 kcal mol^{-1}, while ΔE_{def} is 5.4 and 9.8 kcal mol^{-1}, respectively. The most of the deformation energy is attributed to the cage deformation, with deformation of the fullerenes contributing less than 10%. To analyze the nature of the host–guest interactions, we employed the Morokuma-like interaction energy decomposition analysis[64] implemented in the ADF program.[52] The EDA decomposes the interaction energy into four components: electrostatic (ΔE_{elstat}), Pauli repulsion (ΔE_{Pauli}), orbital interactions (ΔE_{oi}), and dispersion correction (ΔE_{disp}). This decomposition enables us to assess the role of the specific interactions in the systems.

Table 1 represents the EDA analysis results showing similar nature of host–guest interactions in the complexes. Dispersion dominates (63%), followed by electrostatic attraction (24–25%), and orbital interactions (12–13%). The destabilizing term (ΔE_{Pauli}) is 92.6 for $Pt_6PBI_3 \supset C_{60}$ and 112.5 kcal mol^{-1} for $Pt_6PBI_3 \supset C_{70}$. The complex with C_{70} also has higher deformation energy compared to $Pt_6PBI_3 \supset C_{60}$. Overall, based on the complexation energy values, $Pt_6PBI_3 \supset C_{70}$ complex is more stable than $Pt_6PBI_3 \supset C_{60}$, confirming the greater cage affinity to C_{70} observed in the experiment.[43]

We used QTAIM calculations[65] to analyze the host–guest interaction topology in the $Pt_6PBI_3 \supset C_{60}$ and $Pt_6PBI_3 \supset C_{70}$ complexes, considering various topological parameters at BCPs (Table S2, ESI†). Numerical values of these parameters can provide information on the nature of interactions.[66] In both complexes, the analysis revealed only one type of interactions: C···C contacts between fullerene and host cage linkers. These interactions can be described as weak, closed-shell non-covalent interactions. Considering the π-conjugated nature of the guest and **PBI** units, the C···C contacts can be attributed to π···π interactions. No interactions of fullerenes with other metallacage parts were observed due to their spatial separation. In $Pt_6PBI_3 \supset C_{60}$, 11 BCPs for π···π interactions were detected, while replacing C_{60} with C_{70} increases the number of BCPs to 15 in $Pt_6PBI_3 \supset C_{70}$. QTAIM molecular graphs for both complexes are depicted in Fig. S1, ESI.† Considering the similar electron density characteristics at BCPs in both complexes but the higher number of BCPs in $Pt_6PBI_3 \supset C_{70}$, the results correlate well with its stronger interaction energy. The non-covalent interaction (NCI) index analysis[67] showed qualitatively similar NCI isosurface arrangements in both complexes, resembling the metallacage shape. In particular, three distinct areas between **PBI** linkers and fullerene were observed. The reduced density gradient (RDG) plots and NCI isosurfaces are presented in Fig. S2 and S3, ESI.†

Singlet excited states of $Pt_6PBI_3 \supset C_{60}$ and $Pt_6PBI_3 \supset C_{70}$ complexes

Our results revealed relatively low LUMO energy for both the Pt_6PBI_3 cage and C_{60}/C_{70} fullerenes: −3.82 and −2.71/−2.80 eV, respectively (Fig. 1). A very low-lying LUMO of Pt_6PBI_3 suggests its potential as a strong electron acceptor, capable of oxidizing fullerene under photoexcitation. However, study by Fang, Stang, and co-workers indicates only marginal changes in the UV-Vis spectrum of the cage upon fullerene inclusion.[43] To get deeper understanding of the processes taking place under photoexcitation, we performed simulations of excited states using the TDA-DFT method at the CAM-B3LYP-D3(BJ)/def2-SVP//BLYP-D3(BJ)/def2-SVP level of theory (see ESI† for computational details). The TDA-DFT performs well in reproducing experimental absorption and emission spectra of a series of medium-sized conjugated molecules[68] and is computationally feasible method for excited state simulations of large systems. Moreover, the range-separated CAM-B3LYP functional performs well for prediction of excitation energy and is particularly effective in modeling charge transfer processes in fullerene-based complexes, yielding a mean absolute percentage error of 6.3% for charge transfer rate values.[69]

The complexes were split into two fragments: Pt_6PBI_3 and C_{60}/C_{70} fullerene. We examined the electron density distribution for the 40 lowest singlet excited states. These states can be categorized into three types: (1) locally excited (LE) states, in

Table 1 EDA results (in kcal mol^{-1}) for $\mathbf{Pt_6PBI_3}\supset\mathbf{C_{60}}$ and $\mathbf{Pt_6PBI_3}\supset\mathbf{C_{70}}$ complexes at the BLYP-D3(BJ)/TZP level of theory[a]

	Energy terms					ΔE_{def}		
Complex	ΔE_{Pauli}	ΔE_{elstat}	ΔE_{oi}	ΔE_{disp}	ΔE_{int}	Cage	Fullerene	$\Delta E_{complex}$
$\mathbf{Pt_6PBI_3}\supset\mathbf{C_{60}}$	92.57	−37.17 (24%)	−19.88 (13%)	−97.04 (63%)	−61.52	5.14	0.56	−56.10
$\mathbf{Pt_6PBI_3}\supset\mathbf{C_{70}}$	112.52	−47.15 (25%)	−23.39 (12%)	−120.27 (63%)	−78.29	9.41	0.40	−68.48

[a] Relative values (in parentheses) are given as a percentage and express the contribution to the sum of all attractive energy terms: $\Delta E_{elstat} + \Delta E_{oi} + \Delta E_{disp}$. Complexation energy: $\Delta E_{complex} = \Delta E_{int} + \Delta E_{def}$.

which the exciton is mostly localized on either fullerene (LE^{Guest}) or $\mathbf{Pt_6PBI_3}$ (LE^{Host}) with charge separation (CS) below 0.1 *e*; (2) charge transfer (CT) states with significant charge separation (CS > 0.8 *e*); and (3) mixed states, involving both LE and CT contributions (0.1 *e* < CS < 0.8 *e*).

The gas-phase energies of the 40 lowest-lying singlet excited states of $\mathbf{Pt_6PBI_3}\supset\mathbf{C_{60}}$ range from 2.50 to 3.28 eV. The first excited state, at 2.50 eV, corresponds to the LE^{Guest} state with exciton localization on $\mathbf{C_{60}}$ (Table 2). The LE^{Host} state was found at 2.73 eV, *i.e.* 0.23 eV higher in energy compared to LE^{Guest}. The lowest CT state with 0.81 *e* transferred lies at 2.98 eV and can be described as $[\mathbf{Pt_6PBI_3}]^-\supset[\mathbf{C_{60}}]^+$. In the case of $\mathbf{Pt_6PBI_3}\supset\mathbf{C_{70}}$, the first 40 excited states have the energy range from 2.29 to 3.14 eV. The lowest-lying excited state, at 2.29 eV, is the LE^{Guest} state. The energy of the LE^{Host} state is very similar to that in $\mathbf{Pt_6PBI_3}\supset\mathbf{C_{60}}$ and equal to 2.71 eV. Since the HOMO energy of $\mathbf{C_{70}}$ is slightly higher than that of $\mathbf{C_{60}}$, this fullerene should have a slightly improved electron-donor capability. Indeed, the energy of the CT state is 2.63 eV, which is 0.35 eV lower compared to the CT state in the complex with $\mathbf{C_{60}}$. Similar to $\mathbf{Pt_6PBI_3}\supset\mathbf{C_{60}}$, this state results from an electron transfer from $\mathbf{C_{70}}$ fullerene to the metallacage.

To understand how polar environment affects electronic excitations, we used a COSMO-like model[60,61,70–72] with acetonitrile solvent. For the $\mathbf{Pt_6PBI_3}\supset\mathbf{C_{60}}$ and $\mathbf{Pt_6PBI_3}\supset\mathbf{C_{70}}$ complexes, GS dipole moments are 0.87 and 2.11 D, respectively. Their rather small values are due to symmetric structure of the metallacage and fullerene fragments. With Pt(II) centers, *o*-tetrapyridyl **PBI** and triflate counterions, both complexes are expected to have high solvation energies in the GS. In particular, their solvation energies are similar and equal to −5.29 and −5.28 eV. The change in the dipole moment ($\Delta\mu$) due to GS → LE^{Guest}/LE^{Host} excitations is small and hardly exceeds 1 D, keeping the solvation energies in both LE^{Guest} and LE^{Host} states similar to those in the GS. Solvation data for both complexes are given in Table S3, ESI.† The dipole moment changes from GS to CT states are usually much larger than those to LE states due to charge separation. In our study, $\mathbf{Pt_6PBI_3}\supset\mathbf{C_{60}}$ and $\mathbf{Pt_6PBI_3}\supset\mathbf{C_{70}}$ showed relatively small changes, namely 11.84 and 14.47 D, due to high symmetry and efficient charge delocalization. Solvation of the complexes stabilizes CT states, lowering their energies from 2.96 to 2.68 eV and from 2.63 to 2.31 eV for $\mathbf{Pt_6PBI_3}\supset\mathbf{C_{60}}$ and $\mathbf{Pt_6PBI_3}\supset\mathbf{C_{70}}$, respectively.

Table 2 Excitation energies (E_x, eV), main singly excited configuration (HOMO(H)–LUMO(L)) with the largest squared coefficient in the configuration-interaction (CI coef.), oscillator strength (*f*), extent of charge transfer (CT, e) or localization of exciton (*X*) computed for $\mathbf{Pt_6PBI_3}\supset\mathbf{C_{60}}$ and $\mathbf{Pt_6PBI_3}\supset\mathbf{C_{70}}$ complexes in the gas-phase (VAC) and acetonitrile (ACN)

	Supramolecular system			
	$\mathbf{Pt_6PBI_3}\supset\mathbf{C_{60}}$		$\mathbf{Pt_6PBI_3}\supset\mathbf{C_{70}}$	
	VAC	ACN	VAC	ACN
	LE^{Guest} ($\mathbf{C_{60}}$/$\mathbf{C_{70}}$)			
E_x	2.500	2.499	2.289	2.284
Transition (CI coef.)	H−2–L+3 (0.20)	H−1–L+4 (0.24)	H–L+3 (0.45)	H–L+3 (0.48)
f	<0.001	0.001	<0.001	<0.001
X	0.922	0.902	0.930	0.908
	LE^{Host} ($\mathbf{Pt_6PBI_3}$)			
E_x	2.727	2.698	2.711	2.678
Transition (CI coef.)	H−8–L (0.13)	H−5–L+2 (0.20)	H−3–L+2 (0.14)	H−3–L+1 (0.25)
f	0.015	0.027	0.205	0.207
X	0.865	0.868	0.888	0.885
	Most intense absorption band			
E_x	2.792	2.741	2.789[a]	2.739
Transition (CI coef.)	H–L+2 (0.28)	H−5–L+1 (0.27)	H−6–L+5 (0.05)	H−5–L (0.23)
f	1.787	2.199	1.266	1.193
Localization	$\mathbf{Pt_6PBI_3}$	$\mathbf{Pt_6PBI_3}$	$\mathbf{Pt_6PBI_3}$	$\mathbf{Pt_6PBI_3}$
X	0.887	0.860	0.754	0.833
	CT ($\mathbf{C_{60}}$/$\mathbf{C_{70}}$ → $\mathbf{Pt_6PBI_3}$)			
E_x	2.982	2.678	2.632	2.305
Transition (CI coef.)	H−2–L+2 (0.17)	H−4–L+2 (0.21)	H−2–L+2 (0.23)	H−1–L+1 (0.47)
f	0.030	0.027	0.009	0.006
CT	0.813	0.885	0.858	0.928

[a] Mixed state with significant contributions of both LE and CT.

Table 3 Gibbs energy (ΔG^0, in eV), electronic coupling ($|V_{ij}|$, in eV), reorganization energy (λ, in eV), Huang–Rhys factor (S_{eff}), rates (k_X, in s^{-1}) and characteristic time (τ, in ns) for CS and CR processes in **$Pt_6PBI_3 \supset C_{60}$** and **$Pt_6PBI_3 \supset C_{70}$** complexes in ACN

Complex $Pt_6PBI_3 \supset C_{xx}$	Transition	$\Delta G^{0\,a}$	$\lvert V_{ij}\rvert$	λ	$S_{eff}{}^{b}$	k_x	τ
$Pt_6PBI_3 \supset C_{60}$	$LE^{Guest} \rightarrow CT$	0.179	2.34×10^{-3}	0.744	1.26	4.95×10^{6}	202.1
	$CT \rightarrow GS$	−2.678	2.87×10^{-2}	0.724	1.15	7.32×10^{6}	136.6
$Pt_6PBI_3 \supset C_{70}$	$LE^{Guest} \rightarrow CT$	0.021	2.42×10^{-3}	0.683	1.12	3.54×10^{8}	2.8
	$CT \rightarrow GS$	−2.305	1.24×10^{-2}	0.680	1.10	3.23×10^{7}	31.0

[a] Gibbs energy difference between the given states. [b] Effective value of the Huang–Rhys factor $S_{eff} = \lambda_i/\hbar\omega_{eff}$, where $\hbar\omega_{eff}$ is set to 1600 cm^{-1}.

Thus, stabilization of the CT states significantly reduces the energy gap between the CT and the lowest excited state (LE^{Guest}), making CT population possible from this state.

The method of Ulstrup and Jortner[73,74] was employed to estimate charge separation (k_{CS}) and charge recombination (k_{CR}) rates using four parameters, such as electronic coupling of initial and final states (V_{ij}), solvation reorganization energy (λ_s), reaction Gibbs energy (ΔG^0), and Huang–Rhys factor (S_{eff}). We used an effective frequency of 1600 cm^{-1}, corresponding to C=C bond stretching. Testing the effect of the selected frequency on the rate did not reveal significant changes (Table S4, ESI†). The k_{CS} and k_{CR} rates calculated in ACN are listed in Table 3.

In Table 3, **$Pt_6PBI_3 \supset C_{60}$** complex shows charge separation with positive Gibbs energy, taking place in the inverted Marcus region ($|\Delta G^0| > \lambda$). The rate of this process is 4.95×10^6 s^{-1}. At the same time, charge recombination (CT → GS) occurs in a deep inverted Marcus region ($|\Delta G^0| \gg \lambda$). The rates for CS and CR differ by less than two times, with CR surpassing CS. The predicted k_{CS}/k_{CR} ratio suggests that the CT state formation is unlikely in **$Pt_6PBI_3 \supset C_{60}$**. In turn, **$Pt_6PBI_3 \supset C_{70}$** has near-zero Gibbs energy for CS, therefore this process is more thermodynamically favorable than in **$Pt_6PBI_3 \supset C_{60}$**. The CS and CR rates for **$Pt_6PBI_3 \supset C_{70}$** are significantly faster compared to **$Pt_6PBI_3 \supset C_{60}$**, the processes occur in nanoseconds (2.8 ns for CS and 31.0 ns for CR). The slower CR than CS implies a detectable CT state lifetime, although formation of the CT state has not been observed in UV-Vis experiment.[43] The fluorescence measurements for empty metallacage and both complexes with fullerenes show minimal difference in fluorescence decay. The amplitude weighted average fluorescence lifetimes are 2.42, 2.56, and 2.71 ns for **Pt_6PBI_3**, **$Pt_6PBI_3 \supset C_{60}$**, and **$Pt_6PBI_3 \supset C_{70}$**, respectively. Thus, radiative deactivation of excited state is much faster than CT state generation for **$Pt_6PBI_3 \supset C_{60}$** (2.6 ns *vs.* 202.1 ns) and comparable for **$Pt_6PBI_3 \supset C_{70}$** (2.7 ns *vs.* 2.8 ns).

Hence, the absence of experimental detection of the CT state in the studied complexes results from faster radiative deactivation (fluorescence) than CT state formation. Notably, in **$Pt_6PBI_3 \supset C_{60}$**, the formation of the CT state is also slower than non-radiative charge recombination. Fig. 2 highlights the fluorescence and charge transfer processes following photoexcitation of the **$Pt_6PBI_3 \supset C_{60}$** and **$Pt_6PBI_3 \supset C_{70}$**.

Facilitating electron transfer using endohedral metallofullerenes

It is known that an increase in the size of fullerene leads to an increase in its donor abilities. A comparison of the HOMO and LUMO energies of pristine **C_{60}**, **C_{70}**, and **C_{84}** fullerenes (Fig. 3) clearly demonstrates an increase in their HOMO energy from −7.50 eV for **C_{60}** to −7.08 eV for **C_{84}**. The observations made based on the HOMO energy are in a good agreement with the experimentally measured ionization energies of fullerenes, which are equal to 7.57, 7.36, and 7.17 eV for **C_{60}**, **C_{70}**, and **C_{84}**, respectively.[75]

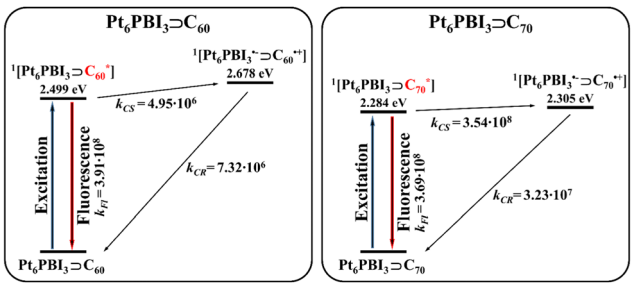

Fig. 2 Summary of the excited state processes for **$Pt_6PBI_3 \supset C_{60}$** and **$Pt_6PBI_3 \supset C_{70}$** in ACN. Fluorescence rates are taken from ref. 43.

As the electron-acceptor properties of **Pt_6PBI_3** proved insufficient to withdraw electron from **C_{60}** and **C_{70}** fullerenes, we hypothesized that replacing these pristine fullerenes with more effective electron donors could facilitate charge transfer. Earlier, we demonstrated that metal nitride endohedral fullerenes effectively donate electrons in complexes with carbon-rich acceptors, such as pristine fullerenes and γ-graphynes.[76,77] Guided by these results, we aimed to evaluate the feasibility of the PET in a series of complexes composed of the **Pt_6PBI_3** metallacage and various endohedral I_h-C_{80}-based metallofullerenes. As it can be seen in Fig. 3, the HOMO energies of endohedral

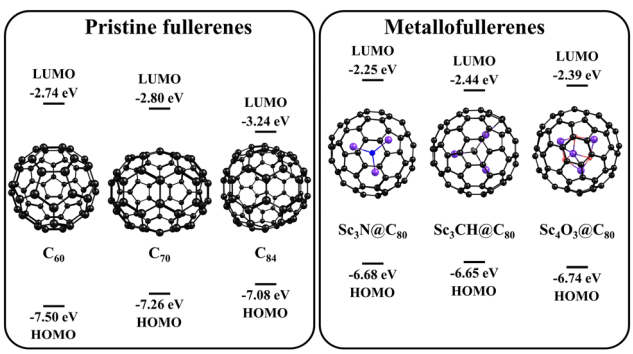

Fig. 3 HOMO and LUMO energies (in eV) of pristine and endohedral metallofullerenes.

metallofullerenes are higher compared to those of the pristine fullerenes of a similar size, suggesting better donor properties, even surpassing those of C_{84} fullerene. This change can be explained by a partial charge transfer between the metal cluster and fullerene cage, thus the electronic structure of the considered metallofullerenes M@C_{80} can be represented as $M^{\delta+}$@$C_{80}^{\delta-}$. Importantly, the host size is suitable to accommodate these metallofullerenes, given their diameter is only 20% larger than that of C_{60}. As cluster-encapsulated fullerenes, we selected three experimentally obtained systems: scandium nitride ($Sc_3N@C_{80}$),[78] hydrogenated scandium carbide ($Sc_3CH@C_{80}$),[79,80] and scandium oxide ($Sc_4O_3@C_{80}$)[81] endohedral fullerenes (Fig. 3). The structures of $Pt_6PBI_3 \supset Sc_3N@C_{80}$, $Pt_6PBI_3 \supset Sc_3CH@C_{80}$, and $Pt_6PBI_3 \supset Sc_4O_3@C_{80}$ were optimized using the BLYP-D3(BJ) functional and def2-SVP basis set.

Given that the metallofullerenes are larger than C_{60} and C_{70}, we first checked the stability of the new complexes. The analysis performed according to the same scheme as for $Pt_6PBI_3 \supset C_{60}$ and $Pt_6PBI_3 \supset C_{70}$ revealed some interesting features of these systems. First, the deformation energy of new complexes is noticeably higher than that of complexes with pristine fullerenes. At the same time, the main contribution to the deformation energy is made by the deformation of metallacage, as in the C_{60} and C_{70} based complexes. Second, the interaction energies are higher compared to $Pt_6PBI_3 \supset C_{60}$ and $Pt_6PBI_3 \supset C_{70}$ due to the larger dispersion correction term. Overall, the complexation energies range from −63.9 to −67.8 kcal mol^{-1} (Table S5, ESI†). Note that the nature of the interactions in all studied complexes is very similar. Thus, the stability of the new complexes is in between of the energy range for $Pt_6PBI_3 \supset C_{60}$ and $Pt_6PBI_3 \supset C_{70}$. Therefore, the binding affinity of the metallacage to the studied fullerenes is in the following order: C_{70} > $Sc_4O_3@C_{80}$ > $Sc_3N@C_{80}$ > $Sc_3CH@C_{80}$ > C_{60}. Since the complexes with pristine fullerenes were successfully synthesized and isolated, we are convinced that the synthesis of the proposed complexes with metallofullerenes is also possible.

Fig. 4 shows that LUMO in all cases is located on one of the **PBI** subunits of the metallacage. Its energy is almost equal to the LUMO energy in $Pt_6PBI_3 \supset C_{60}$ and $Pt_6PBI_3 \supset C_{70}$. In turn, due to the better electron-donor ability of the endohedral metallofullerenes, the HOMO energy in their complexes is in between −7.39 and −7.49 eV, which is higher than the HOMO energies predicted for the complexes with pristine fullerenes (−8.14 and −7.99 eV for $Pt_6PBI_3 \supset C_{60}$ and $Pt_6PBI_3 \supset C_{70}$). In addition, the HOMO in the metallofullerene-based complexes is fully localized on the fullerene, unlike the originally described complexes with pristine fullerenes (Fig. 1). The mentioned differences should facilitate the photoinduced electron transfer in the new systems. To test this assumption, we analyzed the electron density distribution for their 40 lowest singlet excited states.

In all cases, the energies of the excited states in the gas-phase vary from 2.1 to 3.1 eV. The LE state energies of both LE^{Guest} and LE^{Host} turned out to be similar. The CT state in the complexes of interest is characterized by energies from 2.15 to 2.35 eV, depending on the particular complex. It is much lower

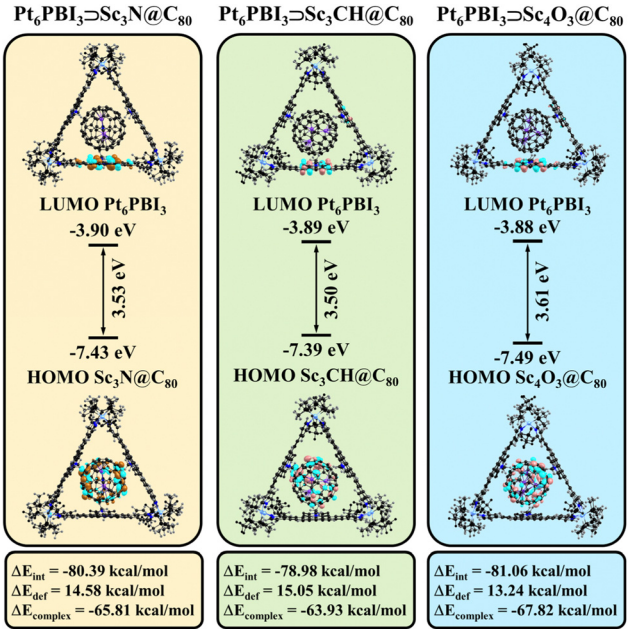

Fig. 4 Structure and HOMO/LUMO energies (in eV) of $Pt_6PBI_3 \supset Sc_3N@C_{80}$, $Pt_6PBI_3 \supset Sc_3CH@C_{80}$, and $Pt_6PBI_3 \supset Sc_4O_3@C_{80}$ complexes.

than the CT state energies in $Pt_6PBI_3 \supset C_{60}$ and $Pt_6PBI_3 \supset C_{70}$ (Table 4). Usually, the energies of the CT states correlate well with the HOMO–LUMO energy gap. It is important to note that for the $Pt_6PBI_3 \supset Sc_3CH@C_{80}$ complex, the CT state is the lowest excited state, even in the gas-phase. For other complexes, the energy difference between the CT state and the lowest LE state, with the exciton localized on the fullerene, does not exceed 0.15 eV. The frontier MOs representing the LE and CT states for

Table 4 Excitation energies (E_x, eV), main singly excited configuration (HOMO(H)–LUMO(L)) with the largest squared coefficient in the configuration-interaction (CI coef.), oscillator strength (f), extent of charge transfer (CT, e) or localization of exciton (X) computed for $Pt_6PBI_3 \supset Sc_3N@C_{80}$, $Pt_6PBI_3 \supset Sc_3CH@C_{80}$, and $Pt_6PBI_3 \supset Sc_4O_3@C_{80}$ complexes in the gas-phase (VAC)

	Supramolecular system		
	$Pt_6PBI_3 \supset XXX@C_{80}$		
	$Sc_3N@C_{80}$	$Sc_3CH@C_{80}$	$Sc_4O_3@C_{80}$
	LE^{Guest} ($XXX@C_{80}$)		
E_x	2.116	2.215	2.235
Transition (CI coef.)	H−4–L+4 (0.77)	H–L+3 (0.86)	H–L+3 (0.37)
f	0.013	<0.001	<005
X	0.923	0.920	0.886
	LE^{Host} (Pt_6PBI_3)		
E_x	2.812	2.747	2.756
Transition (CI coef.)	H−13–L+3 (0.25)	H−7–L ()	H−5–L+2 (0.37)
f	0.446	0.439	0.431
X	0.872	0.881	0.889
	CT ($XXX@C_{80}$ → Pt_6PBI_3)		
E_x	2.260	2.152	2.347
Transition (CI coef.)	H−4–L (0.40)	H–L+2 (0.74)	H−1–L (0.55)
f	0.014	0.013	0.010
CT	0.894	0.883	0.834

the $Pt_6PBI_3 \supset Sc_3N@C_{80}$, $Pt_6PBI_3 \supset Sc_3CH@C_{80}$, and $Pt_6PBI_3 \supset Sc_4O_3@C_{80}$ complexes are shown in Fig. S4–S6, ESI.†

The GS solvation energies of $Pt_6PBI_3 \supset Sc_3N@C_{80}$, $Pt_6PBI_3 \supset Sc_3CH@C_{80}$, and $Pt_6PBI_3 \supset Sc_4O_3@C_{80}$ complexes turned out to be very close to those of the C_{60} and C_{70} based complexes and are equal to −4.83, −5.18, and −5.31 eV, respectively. The difference in dipole moments of the GS and both LE^{Guest} and LE^{Host} states is quite small and does not exceed 3.5 D. As expected, the solvation energies of these LE states are very similar to the solvation energies of GS. At the same time, the difference in dipole moments of GS and CT states in the complexes of interest is large: 10 D for $Pt_6PBI_3 \supset Sc_3N@C_{80}$ and 21 D for $Pt_6PBI_3 \supset Sc_3CH@C_{80}$ and $Pt_6PBI_3 \supset Sc_4O_3@C_{80}$. Subsequently, the difference in solvation energies between GS and CT states is −0.34 eV for the complex with $Sc_3N@C_{80}$, and −0.58 and −0.54 eV for the complexes with $Sc_3CH@C_{80}$ and $Sc_4O_3@C_{80}$. Detailed solvation data in ACN are given in Table S6, ESI.† It is important to note that stabilization of the CT state is sufficient to reorder the LE^{Guest} and CT states in all complexes of interest. Fig. 5 shows the energies of the GS, LE, and CT states in the gas-phase and in ACN, as well as the simulated absorption spectra for all metallofullerene-based complexes.

The higher solvation energy of the CT states in $Pt_6PBI_3 \supset Sc_3CH@C_{80}$ and $Pt_6PBI_3 \supset Sc_4O_3@C_{80}$ compared to the $Sc_3N@C_{80}$ based complex can be explained by different charge delocalization over the host fragment measured by inverse participation ratio (IPR), which counts the number of atoms involved in the charge delocalization. For $Pt_6PBI_3 \supset Sc_3N@C_{80}$, $Pt_6PBI_3 \supset Sc_3CH@C_{80}$, and $Pt_6PBI_3 \supset Sc_4O_3@C_{80}$, the calculated IPR values for the Pt_6PBI_3 host unit are 51.9, 27.5, and 28.4 (see Table S7 for details, ESI†). Charge delocalization over endohedral metallofullerene units is apparently less significant due to their lower accessibility to the solvent. The IPR value for the $Sc_3N@C_{80}$, $Sc_3CH@C_{80}$, and $Sc_4O_3@C_{80}$ units are 30.4, 20.0, and 24.8. Thus, higher charge delocalization and subsequently IPR values for both host and guest subunits in $Pt_6PBI_3 \supset Sc_3N@C_{80}$ are responsible for its lower solvation in the CT state.

According to Table 4, GS → CT transitions in all complexes with metallofullerenes are characterized by a low oscillator strength, making direct population of the CT states through light absorption difficult. However, they can be generated by a decay of LE states. The k_{CS} and k_{CR} rates were calculated using the semi-classical approach.[73,74] The main parameters used in calculation, as well as the rate values are given in Table 5.

Photoinduced electron transfer in the studied complexes is characterized by a negative Gibbs energy in the range from −0.19 to −0.60 eV. The estimated rates of CT generation are very high, thus the process occurs on a picosecond timescale. Characteristic time is 2, 2, and 1 ps, for $Pt_6PBI_3 \supset Sc_3N@C_{80}$, $Pt_6PBI_3 \supset Sc_3CH@C_{80}$, and $Pt_6PBI_3 \supset Sc_4O_3@C_{80}$, respectively. The CR reaction proceeds in a deep inverted Marcus region ($|\Delta G^0| \gg \lambda$) and its rate varies considerably from complex to complex. In particular, for $Pt_6PBI_3 \supset Sc_3N@C_{80}$, charge recombination is almost three orders of magnitude slower than the corresponding charge separation. At the same time, for $Pt_6PBI_3 \supset Sc_3CH@C_{80}$, the charge recombination is only 14 times slower than charge separation. The $Pt_6PBI_3 \supset Sc_4O_3@C_{80}$ complex is located in the middle, with a ratio of charge separation time to charge recombination time of approximately 1 : 150. Considering the fact that PET depends not only on the rate of charge separation, but also on the efficiency of hole and electron extraction, the ideal combination for practical usage is characterized by fast charge separation and slow charge recombination. Therefore, it can be concluded that the $Pt_6PBI_3 \supset Sc_3N@C_{80}$ complex is the best candidate among the considered systems for use as active layer in photovoltaic devices.

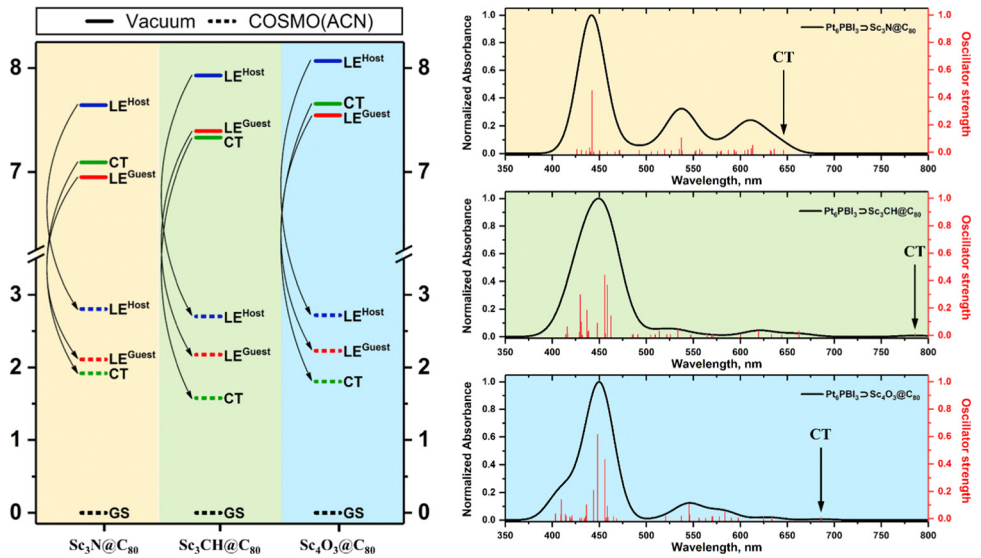

Fig. 5 (Left) Relative energies (in eV) of GS, LE, and CT states of $Pt_6PBI_3 \supset Sc_3N@C_{80}$ (yellow), $Pt_6PBI_3 \supset Sc_3CH@C_{80}$ (green), and $Pt_6PBI_3 \supset Sc_4O_3@C_{80}$ (blue) complexes calculated in vacuum (VAC) and acetonitrile (ACN). (Right) Simulated absorption spectra of the studied complexes in ACN. The spectra were constructed using Gaussian broadening (FWHM = 0.15 eV). Red vertical lines show the oscillator strength for 40 lowest singlet excited states. Vertical arrows correspond to the positions of CT bands in the spectra.

Table 5 Gibbs energy ΔG^0 (in eV), electronic coupling $|V_{ij}|$ (in eV), reorganization energy λ (in eV), Huang–Rhys factor (S_{eff}), activation energy E_a (in eV), rates k_X (in s^{-1}) and characteristic time τ (in ps) for CS and CR processes in **$Pt_6PBI_3 \supset Sc_3N@C_{80}$**, **$Pt_6PBI_3 \supset Sc_3CH@C_{80}$**, and **$Pt_6PBI_3 \supset Sc_4O_3@C_{80}$** calculated in ACN

Complex $Pt_6PBI_3 \supset C_{xx}$	Transition	$\Delta G^{0\,a}$	$\lvert V_{ij}\rvert$	λ	$S_{eff}{}^b$	k_x	τ
$Pt_6PBI_3 \supset Sc_3N@C_{80}$	$LE^{Guest} \rightarrow CT$	−0.191	5.83×10^{-3}	0.412	1.11	4.94×10^{11}	2
	$CT \rightarrow GS$	−1.920	5.25×10^{-2}	0.401	1.05	7.47×10^{8}	1339
$Pt_6PBI_3 \supset Sc_3CH@C_{80}$	$LE^{Guest} \rightarrow CT$	−0.600	5.94×10^{-3}	0.534	1.02	4.95×10^{11}	2
	$CT \rightarrow GS$	−1.577	3.46×10^{-2}	0.531	1.00	3.60×10^{10}	28
$Pt_6PBI_3 \supset Sc_4O_3@C_{80}$	$LE^{Guest} \rightarrow CT$	−0.422	8.85×10^{-3}	0.500	1.11	1.28×10^{11}	1
	$CT \rightarrow GS$	−1.807	5.26×10^{-2}	0.488	1.05	6.49×10^{9}	154

[a] Gibbs energy difference between the given states. [b] Effective value of the Huang–Rhys factor $S_{eff} = \lambda_i/\hbar\omega_{eff}$, where $\hbar\omega_{eff}$ is set to 1600 cm^{-1}, which corresponds to the stretching of C=C bonds.

Conclusions

Using the DFT method, we showed that the **Pt_6PBI_3** metallacage constructed from perylene bisimide units and organoplatinum nodes features an appropriately sized internal cavity, allowing it to form stable complexes not only with pristine **C_{60}** and **C_{70}** fullerenes but also with **$Sc_3N@C_{80}$**, **$Sc_3CH@C_{80}$**, and **$Sc_4O_3@C_{80}$** metallofullerenes. Our calculations reveal that the binding affinities of the studied fullerenes to **Pt_6PBI_3** follows this order: **C_{70}** > **$Sc_4O_3@C_{80}$** > **$Sc_3N@C_{80}$** > **$Sc_3CH@C_{80}$** > **C_{60}**.

The TDA-DFT results indicate that the metallacage has a lower LUMO energy than **C_{60}** and a high ability to delocalize an excess charge, ensuring its excellent electron-acceptor properties. However, the electron affinity of the metallacage is insufficient to withdraw an electron from **C_{60}** or **C_{70}** fullerenes. Charge separation in the **$Pt_6PBI_3 \supset C_{60}$** and **$Pt_6PBI_3 \supset C_{70}$** complexes is characterized by a small positive Gibbs energy and occurs within nanoseconds. Charge recombination is also fast in both complexes, serving as a competitive deactivation channel for the CT state. Moreover, the formation of the CT state in such complexes is hindered by the rapid radiative deactivation channel (fluorescence) of the corresponding LE states, which occurs more quickly than CT state formation.

However, replacing pristine fullerenes with metallofullerenes enables photoinduced electron transfer from fullerene to metallacage, a thermodynamically favorable process occurring within picoseconds. Importantly, in all cases, charge recombination is one to three orders of magnitude slower than the corresponding charge separation. Among the studied complexes, **$Pt_6PBI_3 \supset Sc_3N@C_{80}$** demonstrates the best ratio of fast charge separation and relatively slow charge recombination, making it a highly promising candidate for photovoltaic systems.

Author contributions

O. A. S. investigation, formal analysis, writing – original draft, writing – review & editing. M. S. supervision, writing – review & editing, funding acquisition. A. J. S. investigation, supervision, writing – original draft, writing – review & editing.

Conflicts of interest

There are no conflicts to declare.

Acknowledgements

We are grateful for financial support from the Spanish Ministerio de Ciencia e Innovación (Network RED2018-102815-T, project PID2020-113711GB-I00, and Juan de la Cierva contract IJC2019-039846-I to A.J.S.), the Catalan Conselleria de Recerca i Universitats of the Generalitat de Catalunya (project 2021SGR623) and the University of Girona (María Zambrano fellowship REQ2021_C_31 to O.A.S.). A. J. S. gratefully acknowledges Poland's high-performance computing infrastructure PLGrid (HPC Centers: ACK Cyfronet AGH) for providing computer facilities and support within computational grants no. PLG/2022/016045 and PLG/2022/015981.

References

1 C. J. Pedersen, Cyclic polyethers and their complexes with metal salts, *J. Am. Chem. Soc.*, 1967, **89**(26), 7017–7036.
2 B. Dietrich, J. M. Lehn and J. P. Sauvage, Diaza-polyoxamacrocycles et macrobicycles, *Tetrahedron Lett.*, 1969, **10**(34), 2885–2888.
3 A. Lledó, R. J. Hooley and J. Rebek, Recognition of Guests by Water-Stabilized Cavitand Hosts, *Org. Lett.*, 2008, **10**(17), 3669–3671.
4 F. R. Pinacho Crisóstomo, A. Lledó, S. R. Shenoy, T. Iwasawa and J. Rebek, Recognition and Organocatalysis with a Synthetic Cavitand Receptor, *J. Am. Chem. Soc.*, 2009, **131**(21), 7402–7410.
5 G. Montà-González, F. Sancenón, R. Martínez-Máñez and V. Martí-Centelles, Purely Covalent Molecular Cages and Containers for Guest Encapsulation, *Chem. Rev.*, 2022, **122**(16), 13636–13708.
6 D. Landini, F. Montanari and F. M. Pirisi, Crown ethers as phase-transfer catalysts in two-phase reactions, *J. Chem. Soc., Chem. Commun.*, 1974, **21**, 879–880.
7 D. Vidal, M. Costas, A. Lledó and A. Deep Cavitand, Receptor Functionalized with Fe(II) and Mn(II) Aminopyridine Complexes for Bioinspired Oxidation Catalysis, *ACS Catal.*, 2018, **8**(4), 3667–3672.
8 G. W. Gokel, W. M. Leevy and M. E. Weber, Crown Ethers: Sensors for Ions and Molecular Scaffolds for Materials and Biological Models, *Chem. Rev.*, 2004, **104**(5), 2723–2750.

9 J. Li, D. Yim, W.-D. Jang and J. Yoon, Recent progress in the design and applications of fluorescence probes containing crown ethers, *Chem. Soc. Rev.*, 2017, **46**(9), 2437–2458.
10 H.-J. Schneider and A. K. Yatsimirsky, Selectivity in supramolecular host–guest complexes, *Chem. Soc. Rev.*, 2008, **37**(2), 263–277.
11 F. Cramer, W. Saenger and H. C. Spatz, Inclusion Compounds. XIX.[1a] The Formation of Inclusion Compounds of α-Cyclodextrin in Aqueous Solutions. Thermodynamics and Kinetics, *J. Am. Chem. Soc.*, 1967, **89**(1), 14–20.
12 *Martindale: The Complete Drug Reference*, ed. S. C. Sweetman, Pharmaceutical Press, London, England, UK, 2011.
13 K. Uekama, F. Hirayama and T. Irie, Cyclodextrin Drug Carrier Systems, *Chem. Rev.*, 1998, **98**(5), 2045–2076.
14 T. Wimmer, Cyclodextrines, in *Ullmann's Encyclopedia of Industrial Chemistry*, 2003, DOI: 10.1002/14356007.e08_e02.
15 T. R. Cook, Y.-R. Zheng and P. J. Stang, Metal–Organic Frameworks and Self-Assembled Supramolecular Coordination Complexes: Comparing and Contrasting the Design, Synthesis, and Functionality of Metal–Organic Materials, *Chem. Rev.*, 2013, **113**(1), 734–777.
16 H. Wang, Y. Jin, N. Sun, W. Zhang and J. Jiang, Post-synthetic modification of porous organic cages, *Chem. Soc. Rev.*, 2021, **50**(16), 8874–8886.
17 X. Yang, S. Huang, M. Ortiz, X. Wang, Y. Cao, O. Kareem, Y. Jin, F. Huang, X. Wang and W. Zhang, Truxene-based covalent organic polyhedrons constructed through alkyne metathesis, *Org. Chem. Front.*, 2021, **8**(17), 4723–4729.
18 M. Ortiz, S. Cho, J. Niklas, S. Kim, O. G. Poluektov, W. Zhang, G. Rumbles and J. Park, Through-Space Ultrafast Photoinduced Electron Transfer Dynamics of a C_{70}-Encapsulated Bisporphyrin Covalent Organic Polyhedron in a Low-Dielectric Medium, *J. Am. Chem. Soc.*, 2017, **139**(12), 4286–4289.
19 C. Zhang, Q. Wang, H. Long and W. Zhang, A Highly C_{70} Selective Shape-Persistent Rectangular Prism Constructed through One-Step Alkyne Metathesis, *J. Am. Chem. Soc.*, 2011, **133**(51), 20995–21001.
20 X. Yu, B. Wang, Y. Kim, J. Park, S. Ghosh, B. Dhara, R. D. Mukhopadhyay, J. Koo, I. Kim, S. Kim, I.-C. Hwang, S. Seki, D. M. Guldi, M.-H. Baik and K. Kim, Supramolecular Fullerene Tetramers Concocted with Porphyrin Boxes Enable Efficient Charge Separation and Delocalization, *J. Am. Chem. Soc.*, 2020, **142**(29), 12596–12601.
21 T. R. Cook and P. J. Stang, Recent Developments in the Preparation and Chemistry of Metallacycles and Metallacages via Coordination, *Chem. Rev.*, 2015, **115**(15), 7001–7045.
22 Y. Inokuma, M. Kawano and M. Fujita, Crystalline molecular flasks, *Nat. Chem.*, 2011, **3**(5), 349–358.
23 S. Chakraborty and G. R. Newkome, Terpyridine-based metallosupramolecular constructs: tailored monomers to precise 2D-motifs and 3D-metallocages, *Chem. Soc. Rev.*, 2018, **47**(11), 3991–4016.
24 F. M. Steudel, E. Ubasart, L. Leanza, M. Pujals, T. Parella, G. M. Pavan, X. Ribas and M. von Delius, Synthesis of C_{60}/[10]CPP-Catenanes by Regioselective, Nanocapsule-Templated Bingel Bis-Addition, *Angew. Chem., Int. Ed.*, 2023, **62**(42), e202309393.
25 M. Pan, K. Wu, J.-H. Zhang and C.-Y. Su, Chiral metal–organic cages/containers (MOCs): From structural and stereochemical design to applications, *Coord. Chem. Rev.*, 2019, **378**, 333–349.
26 Y. Sun, C. Chen, J. Liu and P. J. Stang, Recent developments in the construction and applications of platinum-based metallacycles and metallacages via coordination, *Chem. Soc. Rev.*, 2020, **49**(12), 3889–3919.
27 F. J. Rizzuto, L. K. S. von Krbek and J. R. Nitschke, Strategies for binding multiple guests in metal–organic cages, *Nat. Rev. Chem.*, 2019, **3**(4), 204–222.
28 C. García-Simón, M. Costas and X. Ribas, Metallosupramolecular receptors for fullerene binding and release, *Chem. Soc. Rev.*, 2016, **45**(1), 40–62.
29 V. Martínez-Agramunt, S. Ruiz-Botella and E. Peris, Nickel-Cornered Molecular Rectangles as Polycyclic Aromatic Hydrocarbon Receptors, *Chem. – Eur. J.*, 2017, **23**(27), 6675–6681.
30 P. P. Neelakandan, A. Jiménez and J. R. Nitschke, Fluorophore incorporation allows nanomolar guest sensing and white-light emission in M_4L_6 cage complexes, *Chem. Sci.*, 2014, **5**(3), 908–915.
31 J. J. Perry Iv, P. L. Feng, S. T. Meek, K. Leong, F. P. Doty and M. D. Allendorf, Connecting structure with function in metal–organic frameworks to design novel photo- and radioluminescent materials, *J. Mater. Chem.*, 2012, **22**(20), 10235–10248.
32 W. Meng, B. Breiner, K. Rissanen, J. D. Thoburn, J. K. Clegg and J. R. Nitschke, A Self-Assembled M_8L_6 Cubic Cage that Selectively Encapsulates Large Aromatic Guests, *Angew. Chem., Int. Ed.*, 2011, **50**(15), 3479–3483.
33 T. Lin, X. S. Shang, P. N. Liu and N. Lin, Multicomponent Assembly of Supramolecular Coordination Polygons on a Au(111) Surface, *J. Phys. Chem. C*, 2013, **117**(44), 23027–23033.
34 M. Boccalon, E. Iengo and P. Tecilla, Metal–Organic Transmembrane Nanopores, *J. Am. Chem. Soc.*, 2012, **134**(50), 20310–20313.
35 E. Iengo, P. Cavigli, D. Milano and P. Tecilla, Metal mediated self-assembled porphyrin metallacycles: Synthesis and multipurpose applications, *Inorg. Chim. Acta*, 2014, **417**, 59–78.
36 C. García-Simón, C. Colomban, Y. A. Çetin, A. Gimeno, M. Pujals, E. Ubasart, C. Fuertes-Espinosa, K. Asad, N. Chronakis, M. Costas, J. Jiménez-Barbero, F. Feixas and X. Ribas, Complete Dynamic Reconstruction of C_{60}, C_{70}, and $(C_{59}N)_2$ Encapsulation into an Adaptable Supramolecular Nanocapsule, *J. Am. Chem. Soc.*, 2020, **142**(37), 16051–16063.
37 C.-C. You and F. Würthner, Self-Assembly of Ferrocene-Functionalized Perylene Bisimide Bridging Ligands with Pt(II) Corner to Electrochemically Active Molecular Squares, *J. Am. Chem. Soc.*, 2003, **125**(32), 9716–9725.
38 A. Sautter, D. G. Schmid, G. Jung and F. Würthner, A Triangle−Square Equilibrium of Metallosupramolecular Assemblies Based on Pd(II) and Pt(II) Corners and Diazadibenzoperylene Bridging Ligands, *J. Am. Chem. Soc.*, 2001, **123**(23), 5424–5430.
39 V. Blanco, M. D. García, C. Peinador and J. M. Quintela, Self-assembly of new fluorescent Pd(II) and Pt(II) 2,7-

diazapyrenium-based metallocycles and study of their inclusion complexes and [3]catenanes, *Chem. Sci.*, 2011, **2**(12), 2407–2416.
40 S. Lin, X. Chang, Z. Wang, J. Zhang, N. Ding, W. Xu, K. Liu, Z. Liu and Y. Fang, High-Performance NMHC Detection Enabled by a Perylene Bisimide-Cored Metallacycle Complex-Based Fluorescent Film Sensor, *Anal. Chem.*, 2021, **93**(48), 16051–16058.
41 K. Mahata, P. D. Frischmann and F. Würthner, Giant Electroactive M_4L_6 Tetrahedral Host Self-Assembled with Fe(II) Vertices and Perylene Bisimide Dye Edges, *J. Am. Chem. Soc.*, 2013, **135**(41), 15656–15661.
42 P. D. Frischmann, V. Kunz and F. Würthner, Bright Fluorescence and Host–Guest Sensing with a Nanoscale M_4L_6 Tetrahedron Accessed by Self-Assembly of Zinc–Imine Chelate Vertices and Perylene Bisimide Edges, *Angew. Chem., Int. Ed.*, 2015, **54**(25), 7285–7289.
43 X. Chang, S. Lin, G. Wang, C. Shang, Z. Wang, K. Liu, Y. Fang and P. J. Stang, Self-Assembled Perylene Bisimide-Cored Trigonal Prism as an Electron-Deficient Host for C_{60} and C_{70} Driven by ''Like Dissolves Like'', *J. Am. Chem. Soc.*, 2020, **142**(37), 15950–15960.
44 A. D. Becke, Density-functional exchange-energy approximation with correct asymptotic behavior, *Phys. Rev. A: At., Mol., Opt. Phys.*, 1988, **38**(6), 3098–3100.
45 C. Lee, W. Yang and R. G. Parr, Development of the Colle-Salvetti correlation-energy formula into a functional of the electron density, *Phys. Rev. B: Condens. Matter Mater. Phys.*, 1988, **37**(2), 785–789.
46 S. Grimme, J. Antony, S. Ehrlich and H. Krieg, A consistent and accurate ab initio parametrization of density functional dispersion correction (DFT-D) for the 94 elements H-Pu, *J. Chem. Phys.*, 2010, **132**(15), 154104.
47 S. Grimme, S. Ehrlich and L. Goerigk, Effect of the damping function in dispersion corrected density functional theory, *J. Comput. Chem.*, 2011, **32**(7), 1456–1465.
48 F. Weigend and R. Ahlrichs, Balanced basis sets of split valence, triple zeta valence and quadruple zeta valence quality for H to Rn: Design and assessment of accuracy, *Phys. Chem. Chem. Phys.*, 2005, **7**(18), 3297–3305.
49 F. Weigend, Accurate Coulomb-fitting basis sets for H to Rn, *Phys. Chem. Chem. Phys.*, 2006, **8**(9), 1057–1065.
50 ORCA - an ab initio density functional, and semiempirical program package, version 5.0.3.
51 F. Neese, Software update: The ORCA program system—Version 5.0, *Wiley Interdiscip. Rev.: Comput. Mol. Sci.*, 2022, **12**(5), e1606.
52 E. J. Baerends, *et al.*, ADF 2018, Theoretical Chemistry, Vrije Universiteit, Amsterdam, The Netherlands, **https://www.scm.com**.
53 S. Hirata and M. Head-Gordon, Time-dependent density functional theory within the Tamm–Dancoff approximation, *Chem. Phys. Lett.*, 1999, **314**(3), 291–299.
54 T. Yanai, D. P. Tew and N. C. Handy, A new hybrid exchange–correlation functional using the Coulomb-attenuating method (CAM-B3LYP), *Chem. Phys. Lett.*, 2004, **393**(1), 51–57.
55 M. J. Frisch; G. W. Trucks; H. B. Schlegel; G. E. Scuseria; M. A. Robb; J. R. Cheeseman; G. Scalmani; V. Barone; G. A. Petersson; H. Nakatsuji; X. Li; M. Caricato; A. V. Marenich; J. Bloino; B. G. Janesko; R. Gomperts; B. Mennucci; H. P. Hratchian; J. V. Ortiz; A. F. Izmaylov; J. L. Sonnenberg; D. Williams-Young; F. Ding; F. Lipparini; F. Egidi; J. Goings; B. Peng; A. Petrone; T. Henderson; D. Ranasinghe; V. G. Zakrzewski; J. Gao; N. Rega; G. Zheng; W. Liang; M. Hada; M. Ehara; K. Toyota; R. Fukuda; J. Hasegawa; M. Ishida; T. Nakajima; Y. Honda; O. Kitao; H. Nakai; T. Vreven; K. Throssell; J. A. Montgomery.; J. E. Peralta; F. Ogliaro; M. J. Bearpark; J. J. Heyd; E. N. Brothers; K. N. Kudin; V. N. Staroverov; T. A. Keith; R. Kobayashi; J. Normand; K. Raghavachari; A. P. Rendell; J. C. Burant; S. S. Iyengar; J. Tomasi; M. Cossi; J. M. Millam; M. Klene; C. Adamo; R. Cammi; J. W. Ochterski; R. L. Martin; K. Morokuma; O. Farkas; J. B. Foresman and D. J. Fox, *Gaussian 16, Revision A.03*, Gaussian, Inc., Wallingford CT, 2016.
56 R. S. Mulliken, Electronic Population Analysis on LCAO–MO Molecular Wave Functions. I, *J. Chem. Phys.*, 1955, **23**(10), 1833–1840.
57 P. O. Löwdin, On the Non-Orthogonality Problem Connected with the Use of Atomic Wave Functions in the Theory of Molecules and Crystals, *J. Chem. Phys.*, 1950, **18**(3), 365–375.
58 F. L. Hirshfeld, Bonded-atom fragments for describing molecular charge densities, *Theor. Chim. Acta*, 1977, **44**(2), 129–138.
59 A. V. Marenich, S. V. Jerome, C. J. Cramer and D. G. Truhlar, Charge Model 5: An Extension of Hirshfeld Population Analysis for the Accurate Description of Molecular Interactions in Gaseous and Condensed Phases, *J. Chem. Theory Comput.*, 2012, **8**(2), 527–541.
60 A. Klamt and G. Schüürmann, COSMO: a new approach to dielectric screening in solvents with explicit expressions for the screening energy and its gradient, *J. Chem. Soc., Perkin Trans. 2*, 1993, 799–805.
61 A. Klamt, Calculation of UV/Vis Spectra in Solution, *J. Phys. Chem.*, 1996, **100**(9), 3349–3353.
62 T. A. Keith AIMAll, version 19.10.12; TK Gristmill Software: Overland Park, KS, 2019. (**https://aim.tkgristmill.com**).
63 G. A. Zhurko, Chemcraft 1.80 (build 523b) - graphical program for visualization of quantum chemistry computations. (**https://chemcraftprog.com**).
64 K. Morokuma, Why do molecules interact? The origin of electron donor-acceptor complexes, hydrogen bonding and proton affinity, *Acc. Chem. Res.*, 1977, **10**(8), 294–300.
65 R. F. W. Bader, A quantum theory of molecular structure and its applications, *Chem. Rev.*, 1991, **91**(5), 893–928.
66 S. J. Grabowski, What Is the Covalency of Hydrogen Bonding?, *Chem. Rev.*, 2011, **111**(4), 2597–2625.
67 E. R. Johnson, S. Keinan, P. Mori-Sánchez, J. Contreras-García, A. J. Cohen and W. Yang, Revealing Noncovalent Interactions, *J. Am. Chem. Soc.*, 2010, **132**(18), 6498–6506.
68 A. Chantzis, A. D. Laurent, C. Adamo and D. Jacquemin, Is the Tamm-Dancoff Approximation Reliable for the Calculation of Absorption and Fluorescence Band Shapes?, *J. Chem. Theory Comput.*, 2013, **9**(10), 4517–4525.

69 P. Besalú-Sala, A. A. Voityuk, J. M. Luis and M. Solà, Evaluation of charge-transfer rates in fullerene-based donor–acceptor dyads with different density functional approximations, *Phys. Chem. Chem. Phys.*, 2021, **23**(9), 5376–5384.

70 A. J. Stasyuk, O. A. Stasyuk, M. Solà and A. A. Voityuk, Electron Transfer in a Li^+-Doped Zn-Porphyrin–[10]CPP⊃Fullerene Junction and Charge-Separated Bands with Opposite Response to Polar Environments, *J. Phys. Chem. B*, 2020, **124**(41), 9095–9102.

71 A. J. Stasyuk, O. A. Stasyuk, M. Solà and A. A. Voityuk, Photoinduced electron transfer in nanotube⊃C_{70} inclusion complexes: phenine vs. nanographene nanotubes, *Chem. Commun.*, 2020, **56**(83), 12624–12627.

72 A. J. Stasyuk, O. A. Stasyuk, M. Solà and A. A. Voityuk, Photoinduced electron transfer in mechanically interlocked suit[3]ane systems, *J. Mater. Chem. C*, 2021, **9**(30), 9436–9445.

73 J. Ulstrup and J. Jortner, The effect of intramolecular quantum modes on free energy relationships for electron transfer reactions, *J. Chem. Phys.*, 1975, **63**(10), 4358–4368.

74 J. Jortner, Temperature dependent activation energy for electron transfer between biological molecules, *J. Chem. Phys.*, 1976, **64**(12), 4860–4867.

75 O. V. Boltalina, I. N. Ioffe, L. N. Sidorov, G. Seifert and K. Vietze, Ionization Energy of Fullerenes, *J. Am. Chem. Soc.*, 2000, **122**(40), 9745–9749.

76 M. Izquierdo, B. Platzer, A. J. Stasyuk, O. A. Stasyuk, A. A. Voityuk, S. Cuesta, M. Solà, D. M. Guldi and N. Martín, All-Fullerene Electron Donor–Acceptor Conjugates, *Angew. Chem., Int. Ed.*, 2019, **58**(21), 6932–6937.

77 O. A. Stasyuk, A. A. Voityuk, M. Solà and A. J. Stasyuk, γ-graphynes with extended polyyne chains for efficient photoinduced electron transfer in complexes with fullerenes, *Carbon*, 2023, **215**, 118460.

78 S. Stevenson, G. Rice, T. Glass, K. Harich, F. Cromer, M. R. Jordan, J. Craft, E. Hadju, R. Bible, M. M. Olmstead, K. Maitra, A. J. Fisher, A. L. Balch and H. C. Dorn, Small-bandgap endohedral metallofullerenes in high yield and purity, *Nature*, 1999, **401**(6748), 55–57.

79 M. Krause, F. Ziegs, A. A. Popov and L. Dunsch, Entrapped Bonded Hydrogen in a Fullerene: the Five-Atom Cluster Sc_3CH in C_{80}, *ChemPhysChem*, 2007, **8**(4), 537–540.

80 K. Junghans, M. Rosenkranz and A. A. Popov, $Sc_3CH@C_{80}$: selective ^{13}C enrichment of the central carbon atom, *Chem. Commun.*, 2016, **52**(39), 6561–6564.

81 S. Stevenson, M. A. Mackey, M. A. Stuart, J. P. Phillips, M. L. Easterling, C. J. Chancellor, M. M. Olmstead and A. L. Balch, A Distorted Tetrahedral Metal Oxide Cluster inside an Icosahedral Carbon Cage. Synthesis, Isolation, and Structural Characterization of $Sc_4(\mu_3\text{-}O)_2@I_h\text{-}C_{80}$, *J. Am. Chem. Soc.*, 2008, **130**(36), 11844–11845.